Iraqi Journal of Physics, 2023 *Vol. 21, No.3, PP. 9-23*

https://doi.org/10.30723/ijp.v21i3.1122

P-ISSN: 2070-4003
E-ISSN: 2664-5548

Investigation of Numerical Simulation for Adaptive Optics System

Sara Usama Jasim[1a*] and Raaid Nawfee Hassan[1b]
[1]*Department of Astronomy and Space, College of Science, University of Baghdad. Baghdad, Iraq*
[b]E-mail: raaid.hassan@sc.uobaghdad.edu.iq
[a*]Corresponding author: sara.usama1207m@sc.uobaghdad.edu.iq

Abstract

In this study, the performance of the adaptive optics (AO) system was analyzed through a numerical computer simulation implemented in MATLAB. Making a phase screen involved turning computer-generated random numbers into two-dimensional arrays of phase values on a sample point grid with matching statistics. Von Karman turbulence was created depending on the power spectral density. Several simulated point spread functions (PSFs) and modulation transfer functions (MTFs) for different values of the Fried coherent diameter (r_o) were used to show how rough the atmosphere was. To evaluate the effectiveness of the optical system (telescope), the Strehl ratio (S) was computed. The compensation procedure for an AO system was implemented. Analytical analysis was used to define the wave front and aberrations of the circular aperture telescope. Zernike polynomials were used to describe the residual error and figure out how much the compensation changed the measured turbulence values. The results of the computer simulation involving atmospheric turbulence reveal that elevating the r_o values (4, 8, 12, 16, 20, 24, 28, 32) cm resulted in a 3.4% rise in S. However, when the adaptive optics system operated with a constant r_o (20 cm), augmenting the Zernike aberration modes led to a remarkable 44% increase in S, signifying a substantial enhancement in the compensation procedure.

Article Info.

Keywords:
Adaptive Optics, Power Spectral Density, Von Karman turbulence, Zernike polynomials, Atmospheric turbulence.

Article history:
Received: Apr. 12,2023
Revised: Jun. 25, 2023
Accepted: Jun. 27, 2023
Published: Sep. 01,2023

1. Introduction

Adaptive optics (AO) is a technique which eliminates aberrations from optical systems by using at least one deformable mirror which alters its shape to account for the aberrations [1]. The real-time aberration of light in optical systems is corrected using AO [2]. In ground-based telescope applications, atmospheric turbulence can drastically decrease resolution for pupil diameters much bigger than Fried coherence diameter (r_o) [3]. A telescope equipped with a functional adaptive optics system enhances the spatial resolution of the image [4]. Light collected by ground-based telescopes has propagated through turbulent Earth atmosphere before arriving at the Earth's surface. Because of this, initially, parallel light waves are distorted because environmental and internal factors affect the system light waves propagating through the atmosphere. Index of refraction variations arises from fluctuations of temperature, air density, pressure, observed wavelengths band, atmospheric parameters (such as Fried coherence parameter and atmospheric time constant), and telescope parameters (such as aperture diameter and telescope field of view) [5]. Temperature inhomogeneity is produced when layers of different temperatures are mixed due to wind shears. The statistics of refractive index inhomogeneities follow the temperature inhomogeneities described by Kolmogorov [6-8].

The aim of the research is to study the adaptive optics system and the compensation mechanism for mitigating the effects of atmospheric turbulence on the clarity and quality of the observed images through numerical computer simulation.

Iraqi Journal of Physics by IJP is licensed under a Creative Commons Attribution 4.0 International License.

2. Atmospheric Turbulence Parameters

The wave-front of light beam arriving from distant astronomical sources is aberrated after passing through the turbulent layers of the Earth's atmosphere. The spatial and temporal inhomogeneities in the refractive-index of the air along the beam path produce random phase perturbations, impairing the performance of ground-based telescopes. The influence of wave-front distortion on optical system was investigated by Fried (1965, 1966) using Kolmogorov's model of turbulence [9, 10].

Since this turbulence model depends on Kolmogorov's theory of turbulence, it is frequently used to explain the impacts of seeing on telescope imaging. It is the source of the formalism used here. The two main factors that cause seeing error in telescopes are (i) vertical movement of the air that is brought on by warmer air rising and mixing with the cooler air above, (ii) upper-level winds that carry this relatively slow-changing turbulent structure made up of air pockets with varying sizes, temperatures, and refractive indices across aperture window. Variations in the temperature lead to changes in refractive index, which cause delay or advance points on the wave front, thus losing its shape. Wave front roughness is primarily caused by small-scale differences in air optical characteristics at the level of smaller turbulent cells. Fig.1 shows the problem of wave front distortion and reduction in resolution arising from atmospheric turbulence. Wave front tilt deformation is caused by temperature/index fluctuation at bigger scales [11-13].

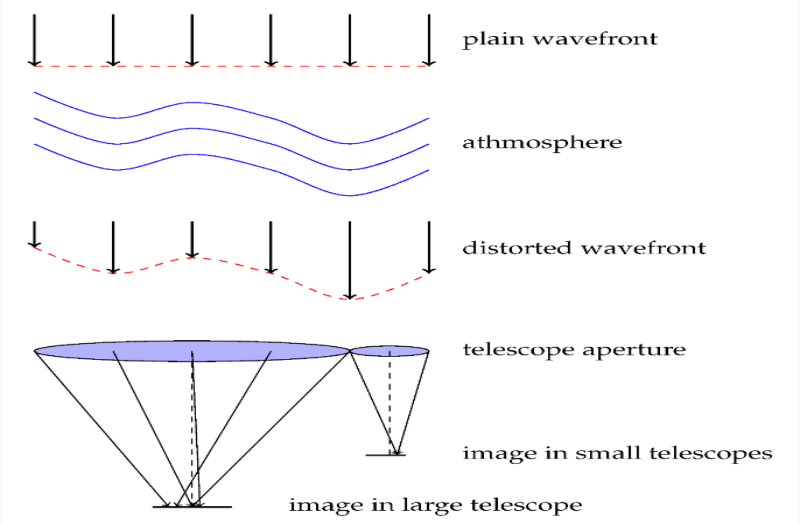

Figure 1: Resolution drop of an image of a point source due to atmospheric turbulence [9].

While large apertures are more susceptible to speckles, small mirror diameter telescopes are more susceptible to the tip-tilt effect [14]. The related structural functions provide a statistical definition for variations from uniformity in the refractive index, wave, and phase [15]. Over millisecond time intervals, the speckle pattern essentially does not change. According to the height of the dominant turbulence layer and the amount of turbulence, two speckle patterns can only be identical at a solid angle, the isoplanatic angle, of a few arc seconds [16]. The isoplanatic angle (θ_0), also known as Roddier's angle, is deduced from the spatio-angular correlation of phase complex amplitudes of two-point sources separated by this angle [17]. The standard definition of the atmospheric isoplanatic angle is [18, 19]:

$$\theta_o = 0.31 \frac{r_o}{h} \qquad (1)$$

where: r_o represents Fried parameter, h represents the height of the turbulence. For r_o and h measured in meters, the isoplanatic angle is in arc seconds [20].

Additionally, every given speckle pattern retains its virtually constant appearance for a very short time, known as the coherence time. The coherence time, τ_o, the time for the Root Mean Square (RMS) phase error to reach 1 rad, is dependent on the direction and speed of the wind and can be shown by the following equation [21, 22]:

$$\tau_o = t_2 - t_1 = 0.314 \frac{r_o}{v} \qquad (\mathbf{2})$$

where: v represents the speed of the wind in dominate layer. This definition results in the same wavelength dependence for $\tau_o$and r_o. The speed values of the wind can generally be of approximately 20m/sec. With the usual r_o values of about 20cm, at good observing sites, $\tau_o$is equal to 10ms [23, 24]. Fig.2 shows a schematic diagram of the definition of Fried parameter, atmospheric time constant, and isoplanatic angle in Fig. 2.

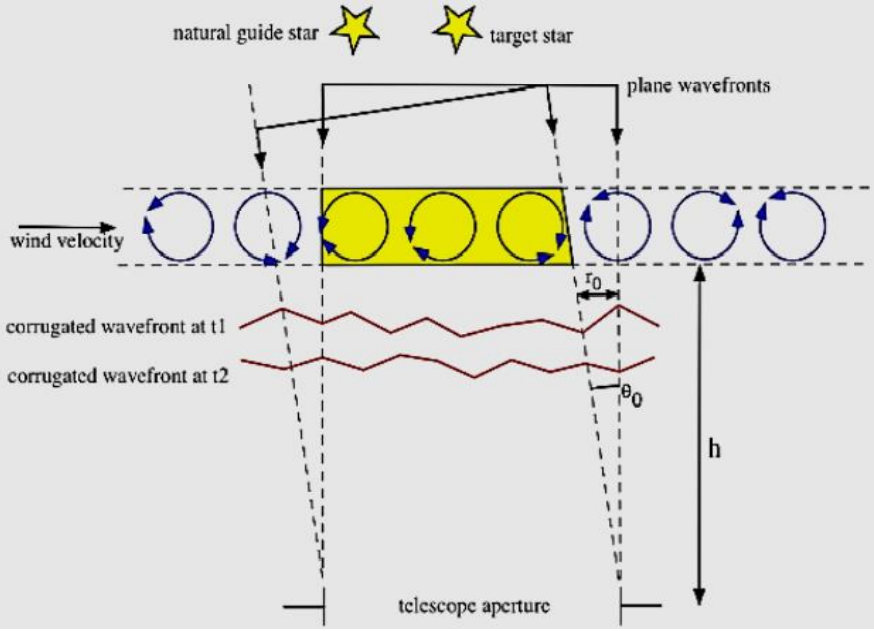

Figure 2: A schematic diagram displaying the definition of the Fried parameter, the atmospheric time constant, and isoplanatic angle [19].

3. Power Spectral Models

The outer turbulence scale (L_o) was estimated to be in the order of a few meters to tens of meters, which is of similar order to the aperture size of large telescopes. L_o is determined by directly sensing wave front on various length scales and fitting a model to observations [25, 26].

For Kolmogorov turbulence, the power spectral density of the fluctuations of refractive index is given by the Kolmogorov power spectrum [27-29]:

$$\Phi_n(\vec{k}) \cong 0.033 C_N^2(z) k^{\frac{-11}{3}} \qquad {}^1/_{L_o} < k < {}^1/_{l_o} \qquad (\mathbf{3})$$

where: k is the transverse wavenumber which is inversely related to the size of the turbulent eddies in the atmosphere. The spectrum has a straightforward structure and relies only on its refractive structure constant C_N^2. For integration throughout the entire spatial frequency spectrum, the outer scale often is set to $L_o = \infty$ and the inner scale is set to $l_o = 0$. In an image plane of a large telescope, there is less image motion than expected

by the Kolmogorov model. Von Karman recognized the issue and updated Kolmogorov's power spectrum for refractive index fluctuations [30, 31]. Von Karman had modified Kolmogorov power spectrum for the purpose of attenuating low spatial frequency values [32]; both spectra are plotted in Fig.3. The Von Karman spectrum has the form [33-35]:

$$\Phi_n(\vec{K}) \cong 0.033\, C_N^2 (K^2 + K_o^2)^{\frac{-11}{6}}\, exp\, exp\, (-K^2 + K_m^2) \qquad (\mathbf{4})$$

where: K_m=5.29/l_0 represents the equivalent wave-number of the inner scale, K_o=2π/L_o represents the outer scale wave-number, K represents unbounded non-turbulent wave number in medium. The shape of this power law informs the design of AO system.

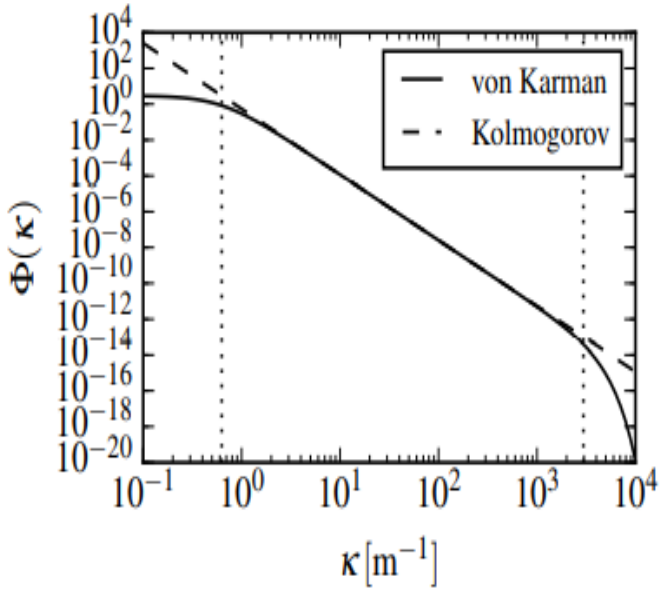

Figure 3: Power spectral density for Von Karman and Kolmogorov turbulence [24].

4. Point Spread Function and Modulation Transfer Function Calculations

The point object image, which is produced by optical system has been referred to as the impulse response or the Point Spread Function (PSF). It can be represented by [36-38]:

$$PSF((sin\ sin\ \theta_x), (\ sin\ sin\ \theta_y)) = \frac{\lambda^2}{Ap} . \| FT \left\{ P\left(\frac{x}{\lambda}, \frac{y}{\lambda}\right) . e^{-i\frac{2\pi}{\lambda} w\left(\frac{x}{\lambda}, \frac{y}{\lambda}\right)} \right\} \|^2 \qquad (\mathbf{5})$$

where: FT represents Fourier Transform Operator, A_P represents the area of exit pupil, $e^{-i\frac{2\pi}{\lambda}}$ and represents the phase deviations of wave-front from reference sphere.

$$PSF(\theta_x, \theta_y) \cong \frac{\lambda^2}{Ap} \| FT \left\{ P\left(\frac{x}{\lambda}, \frac{y}{\lambda}\right) . e^{-i\frac{2\pi}{\lambda} w\left(\frac{x}{\lambda}, \frac{y}{\lambda}\right)} \right\} \|^2 \qquad (\mathbf{6})$$

For Small Angels $P\left(\frac{x}{\lambda}, \frac{y}{\lambda}\right)$ defines shape, size (in wavelengths units), and exit pupil transmission $\frac{Ap}{\lambda^2}$ is exit pupil area in (wavelength)^2 units. $e^{-i\frac{2\pi}{\lambda} w(\frac{x}{\lambda}, \frac{y}{\lambda})}$ represents the deviations of the phase of the wave front from reference sphere, *W(x,y)* represents the wave aberration function at exit pupil, OTF represents the Optical Transfer Function, MTF is the Modulation Transfer Function which can be written as [39-43]:

$$OTF(s_x, s_y) = \frac{FT\{PSF(\theta_x,\theta_y)\}}{FT\{PSF(\theta_x,\theta_y)\}|_{s_x=0,\, s_y=0}} \quad (7)$$

$$MTF(s_x, s_y) = \|OTF(s_x, s_y)\| \quad (8)$$

s_χ is in units of cycle/radian, s_y is in cycle/radian units.

5. Strehl Ratio

The Strehl Ratio (S) is used to evaluate the effectiveness of the optical system. *S* is always between 0 and 1 in a real optical system. It is defined as the peak intensity ratio of measured PSF to the peak intensity of the perfect diffraction-limited (PSF0) for the same optical system [44, 45].

$$S = \frac{max(PSF)}{max(PSF0)}. \quad (9)$$

Also, according to the following, the pupil phase variance is what determines an image's *S* value [46]:

$$S = exp(-\sigma_\varphi^2), \quad (10)$$

where: σ_φ^2 represents the variance of the phase φ as determined by (rad^2). *S* may be calculated by the so-called extended Marechal approximation [47]:

$$S = e^{-1.03(\frac{D}{r_o})^{5/3}} \quad (11)$$

It shows that the Strehl ratio for the images obtained with telescope of diameter $D = r_o$ is $S = 0.360$; for $D > r_o$ the Strehl ratio precipitously decreases with the diameter of the telescope [48, 49].

In Fig. 4, "S" represents a measure of how close the image is to the theoretical diffraction limit. It quantifies the image quality or resolution achieved by the system, with higher values of "S" indicating that the image is closer to the ideal diffraction-limited performance [50].

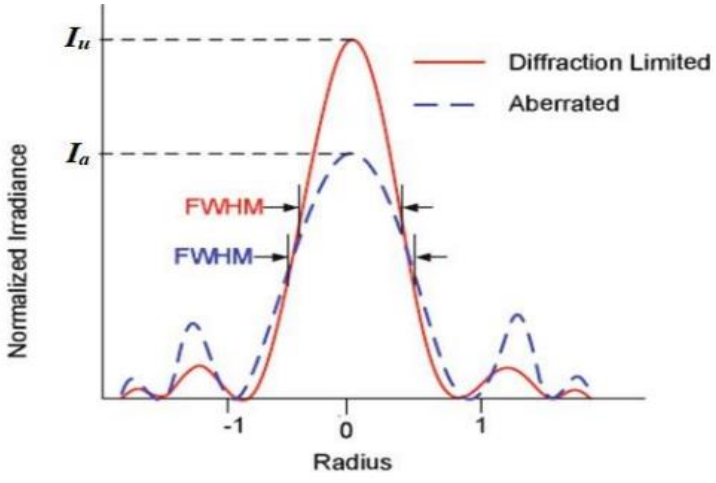

Figure 4: Illustration of a 2D point spread function, Strehl Ratio, and FWHM [30].

6. Results and Discussion

A computer simulation of an optical telescope with a circular aperture was designed. The simulation was carried out for several different effects of turbulence strength using the Von Karman model mentioned in Eq. (4). They alter the shape and size of the impulse response, or PSF, of the optical system, which distorts the image. Turbulence effects can thus be characterized by calculating of the MTF of the PSF and the *S* of the optical system. Also, AO system compensation was simulated, depending on Zernike polynomials.

6.1. Numerical Simulation Steps

This section includes the results of the numerical simulation for the profiling of the wave front beam propagation via atmosphere turbulent medium as follows:

1. Aperture simulation with a telescope of a diameter of 512 pixels and a wavelength of 500 nm and r_o=10cm, as shown in Fig. 5.

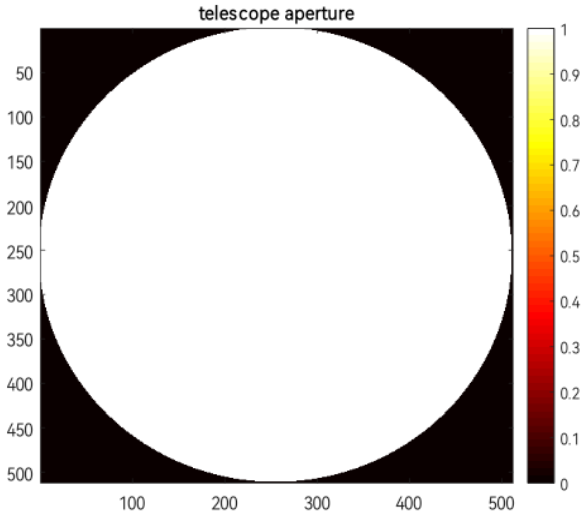

Figure 5: Aperture of telescope.

2. Preliminary grid set-up and constants: number of sample points N = 2^{10}, inner scale l_o= 0.01m, and outer scale L_o=300m. The physical size of the grid is 0.75, and samples size is $0.5x10^{-3}$.
3. Turbulence creation using power spectrum density for the Von Karman model is shown in Fig. 6.

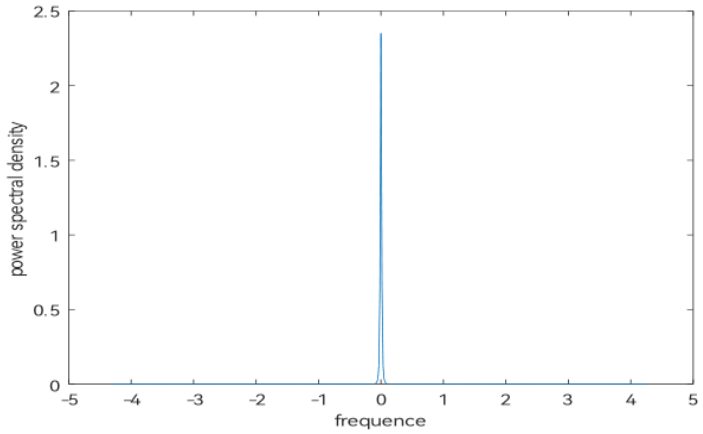

Figure 6: Power spectrum density for Von Karman model.

4. Random coefficient generation using the MATLAB function (randn) is shown in Fig.7.

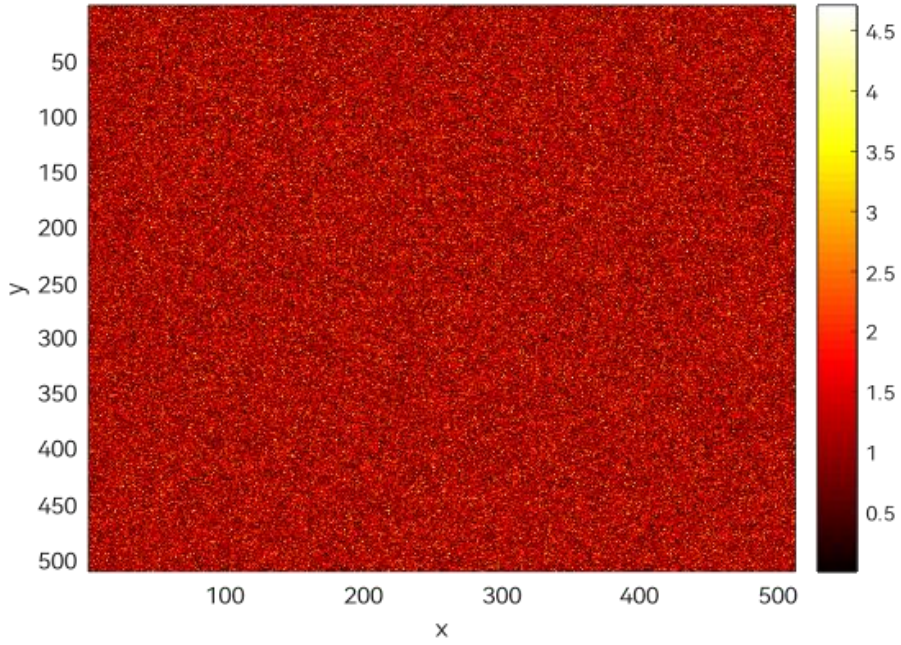

Figure 7: Random number generation.

5. Phase screen generation was performed by the real part of the Fourier transform for the square root power spectral density multiplied by the random coefficients, as shown in Fig.8.

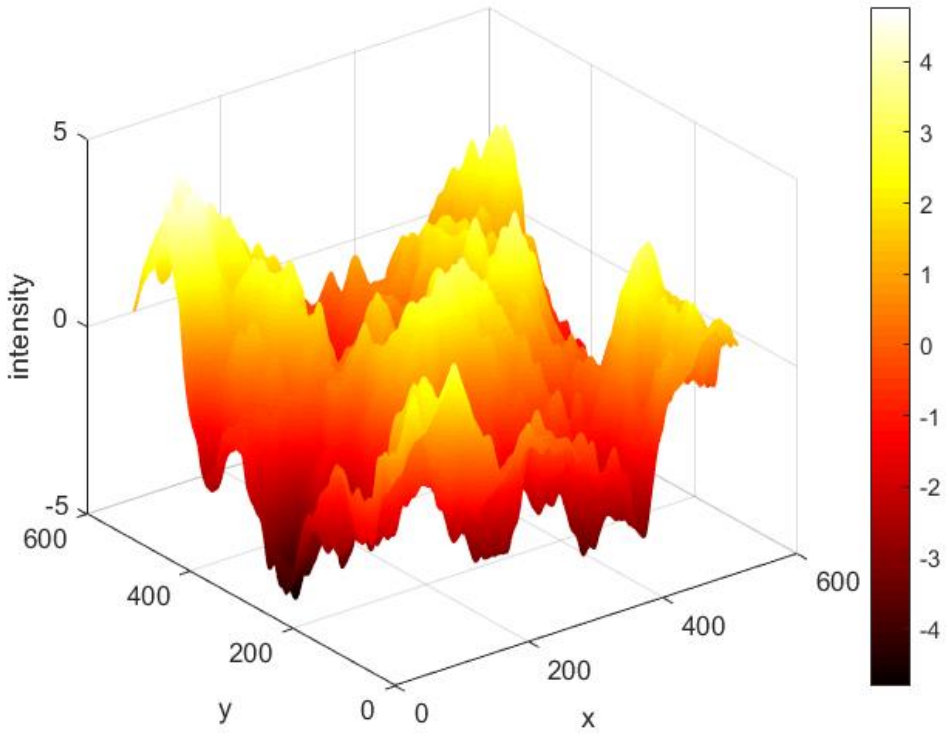

Figure 8: Phase screen for Van Karman model

6. The phase screen fit for the telescope's circular aperture for Von Karman turbulence is shown in Fig.9.

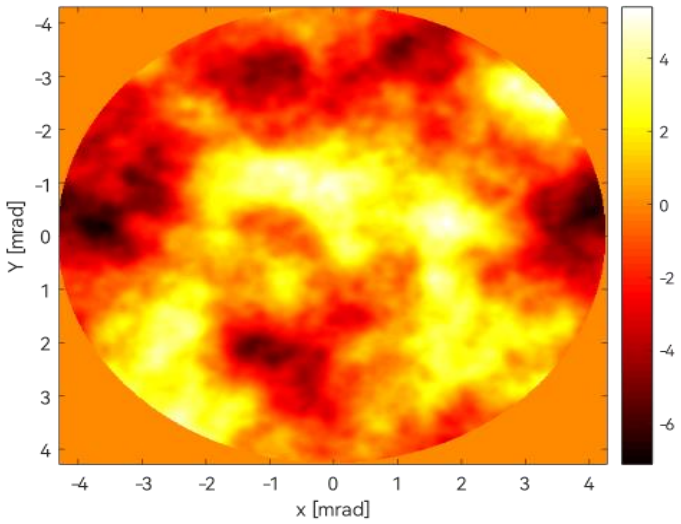

Figure 9: Phase screen fit to telescope aperture

7. The quality of the optical system determined by computing PSF with and without turbulence according to Eq. (5) is shown in Figs.10 and 11.

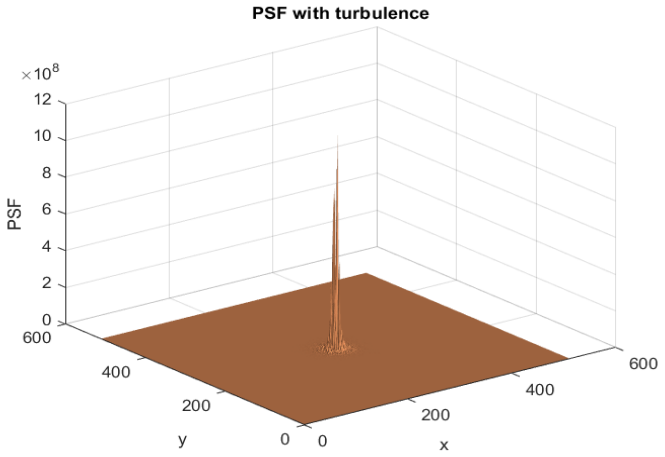

Figure 10: PSF with turbulence.

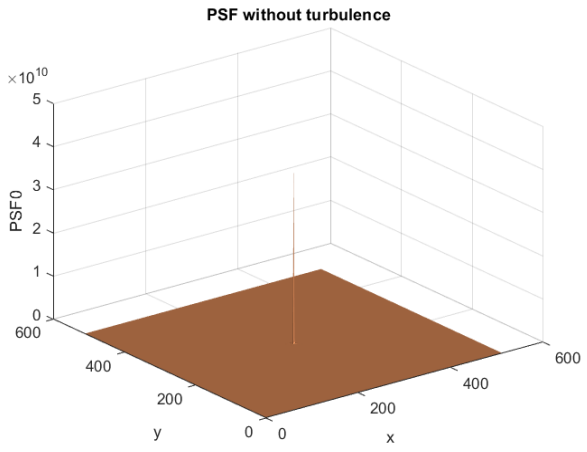

Figure 11: PSF without turbulence.

8. The Modulation Transfer Function (MTF) in cycles per millimeter (cycle/mm) was plotted for a telescope with and without turbulence, represented by the red curve and the blue curve, respectively. This was done using Equations (7 and 8) and is shown in Fig. 12, with different values of " r_o " serving as an indication of the turbulence's strength. Small values of " r_o " indicate strong turbulence, leading to poor seeing, while large values correspond to weak turbulence, resulting in good seeing.

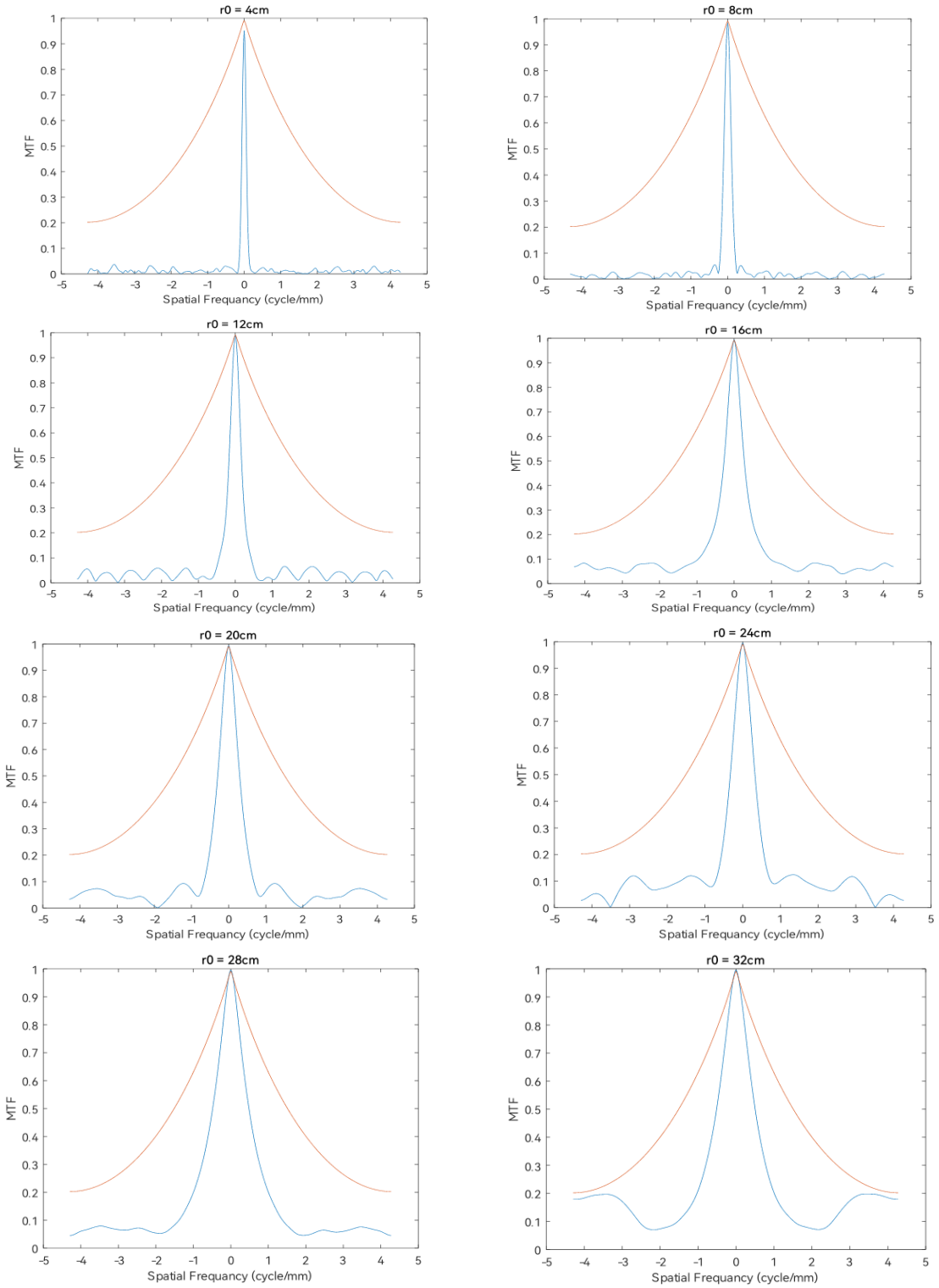

Figure 12: Normalized MTF; red curve with turbulence and blue curve without turbulence. For r_0 = 4, 8, 12, 16, 20, 24, 28, 32 cm.

The red-line MTF represents the ideal optical system without any aberrations. In general, from Fig.12, it can be observed that the MTF shape suffers more distortion and higher phase fluctuation in the case of strong turbulence compared to weak turbulence. The blue MTF curve of r_o =4cm is the most perturbed case and has the smallest area under the curve. When r_o was increased, the MTF blue curve also increased.

The increasing relationship between Strehl ratio (S) and Fried coherent diameter (r_o) (from 4 to 32 cm) with turbulence was plotted using Eq. (9), as shown in Fig.13.

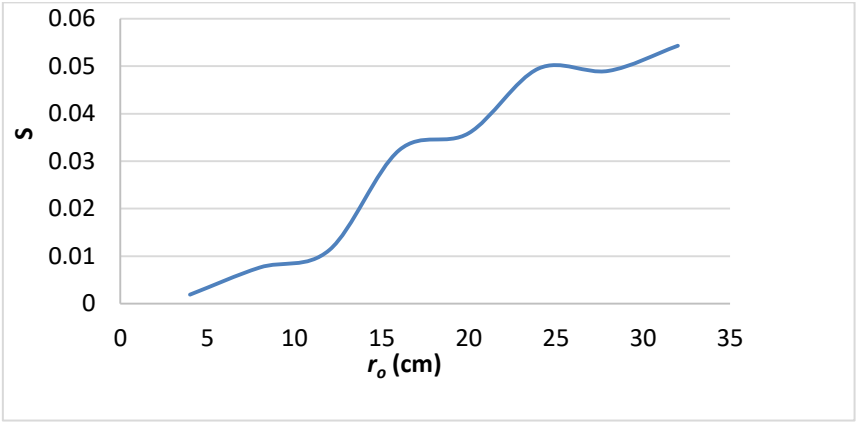

Figure 13: Preoperational relationship between Strehl ratio (S) and Fried coherent diameter (r_o) in the presence of turbulence.

9. Aberration creation using Zernike polynomials for the Von Karman turbulence model was divided into three cases, as shown in Figs.14, 16, and 18, which represent phase screen retrieval. The wave front under test was generated using Zernike polynomial expression, demonstrating that there was still a considerable difference between the original wave front and the simulation result.

   This difference diminished as the number of aberration modes increased. Figs. 15, 17, and 19 show the Zernike coefficient that represents the command matrix of the deformable mirror's actuators in the AO system.

   As evident from these figures, when the aberration modes increased, the high-order aberrations (occurring at lower spatial scales) demonstrated a noticeable impact on the compensated aberration. The Strehl ratio values exhibited increments of 0.2, 0.38, and 0.74.

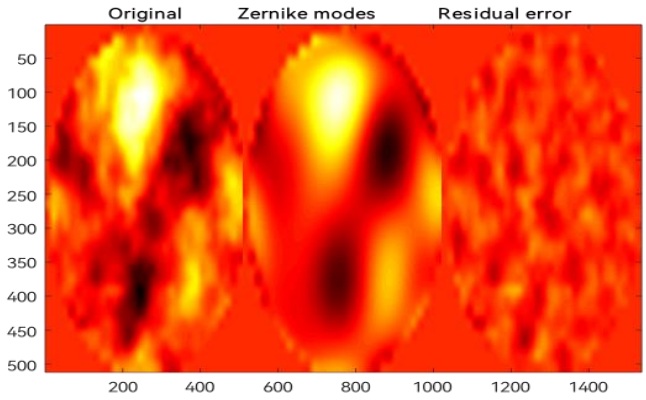

Figure 14: The residual error between the original phase screen and the compensated wave front using Zernike polynomials with 4 aberration modes.

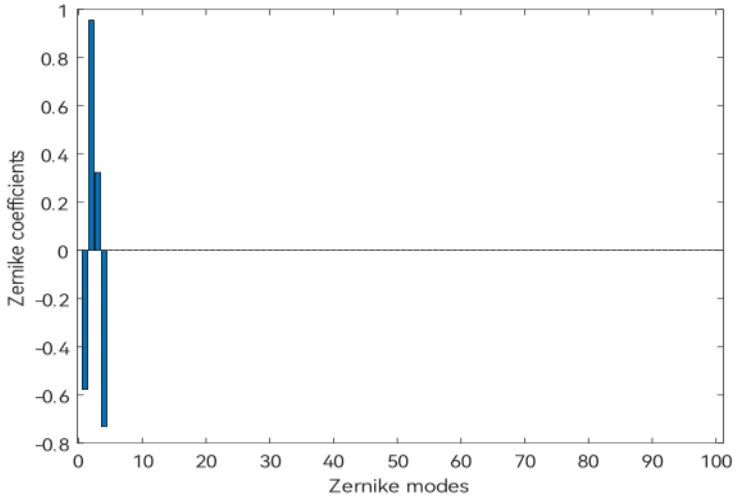

Figure 15: Zernike coefficients for 4 aberration modes.

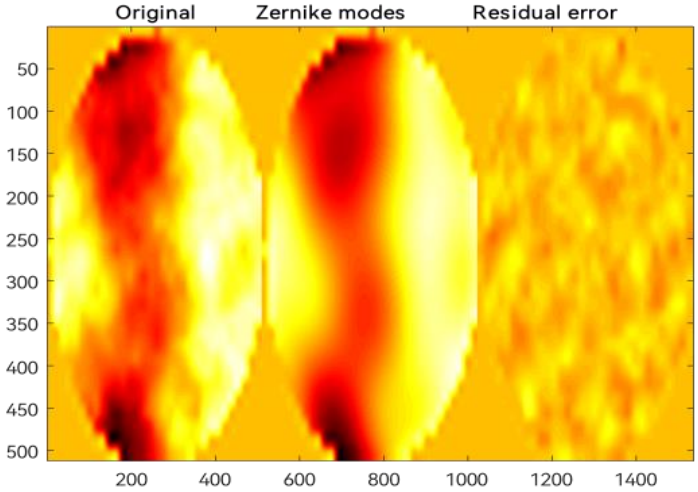

Figure 16: The residual error between the original phase screen and the compensated wave front using Zernike polynomials with 10 aberration modes.

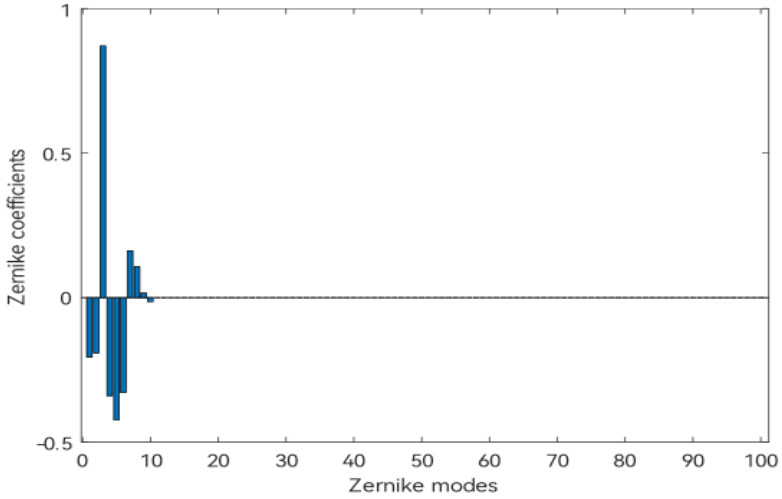

Figure. 17: Zernike coefficients for 10 aberration modes.

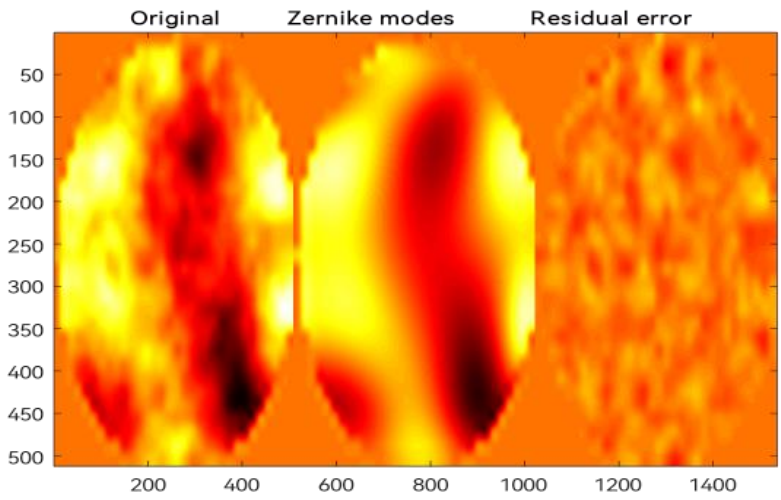

Figure 18: The residual error between the original phase screen and the compensated wave front using Zernike polynomials with 50 aberration modes.

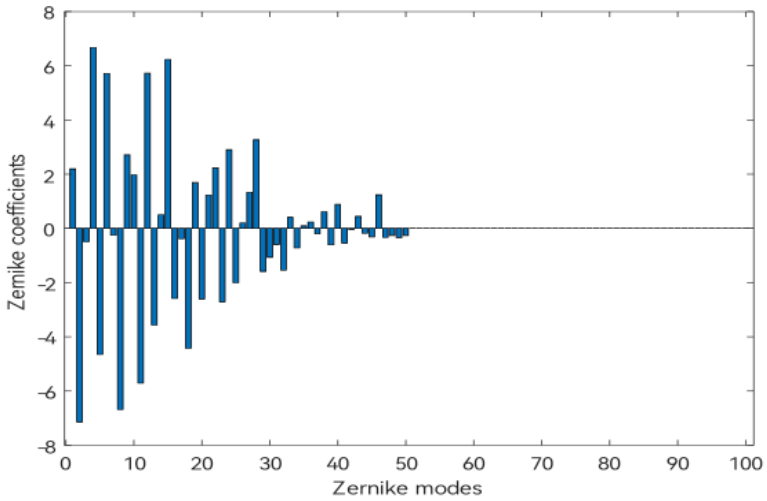

Figure 19: Zernike coefficients for 50 aberration modes.

7. Conclusions

The investigation involved numerical simulations of various aspects of the adaptive optics (AO) system for telescopes. Firstly, aberrated wave fronts were described using Zernike polynomials for a circular aperture. The strength of atmospheric turbulence and seeing conditions significantly affected image quality, emphasizing the importance of atmospheric parameters during observations (e.g., r_o = 20 cm). The AO system compensated for Von Karman atmospheric turbulence using different aberration modes represented by Zernike polynomials (4, 10, and 50 modes). The number of Zernike coefficients determined the actuator forces for the correction mirror.

Important parameters, such as r_o, MTF, PSF, and *S*, were employed to characterize simulated atmospheric turbulence. The study aimed to achieve optimal optical resolution or Strehl ratio for corrected images through modal compensation of atmospheric turbulence. For high-order Zernike modes, the Strehl ratio of compensation often exceeded the exponential function of the negative residual error.

Two cases were considered: the first focused on the Strehl ratio as a function of r_o with turbulence, resulting in marginal improvement. In contrast, the second case explored the Strehl ratio as a function of the number of aberration modes being

compensated, leading to substantial improvements. Overall, the simulation provided valuable insights into enhancing image quality and correcting atmospheric distortions in AO systems. Based on the aforementioned conclusions, the workings of the AO system were convincing and resulted in a diffraction-limited image, as well as an improvement quantified by other optical performance metrics.

Acknowledgements

The authors would like to thank the University of Baghdad, the College of Science, Department of Astronomy and Space for financial support for this study.

Conflict of interest

Authors declare that they have no conflict of interest.

References

1. P. D. V. Pereira, B. Holden, R. Morgan, J. Gubner, T. J. Murphy, C. Haughwout, G. Allan, Y. Xin, W. Kammerer, and K. Cahoy, in 34th Annual Small Satellite Conference, Utah State University, Logan, UT, 2020, p. 121.
2. J. Liu, V. A. Muruganandan, R. Clare, M. C. R. Trujillo, and S. J. Weddell, in 35th International Conference on Image and Vision Computing New Zealand, IEEE, 2020, p. 1.
3. A. Y. Shikhovtsev, P. G. Kovadlo, V. B. Khaikin, V. V. Nosov, V. P. Lukin, E. V. Nosov, A. V. Torgaev, A. V. Kiselev, and M. Y. Shikhovtsev, Remot. Sens. **14**, 1833 (2022).
4. P. Hickson, J. Hellemeier, and R. Yang, Opt. Lett. **46**, 1792 (2021).
5. A. Y. Shikhovtsev, L. Bolbasova, P. Kovadlo, and A. Kiselev, Mon. Nots. Roy. Astro. Soci. **493**, 723 (2020).
6. R. N. Hassan, Neuro Quantol. **20**, 574 (2022).
7. R. V. Sreekanth, R. K. Banyal, R. Sridharan, and A. Selvaraj, Res. Astron. Astrophys. **19**, 074 (2019).
8. W. W. Arrasmith, *Systems Engineering and Analysis of Electro-Optical and Infrared Systems*. 1st Ed. (Boca Raton, CRC Press, 2018).
9. A. Popowicz and V. Orlov, Sensors **22**, 7902 (2022).
10. U. E. Jallod, Iraqi J. Sci. **58**, 583 (2017).
11. R. N. Hassan, H. S. Ali, and W. H. Wadee, Iraqi J. Sci. **62**, 2463 (2021).
12. Y. Yan, S. Wu, L. Shi, W. Li, J. Si, and H. Niu, in Optical Metrology and Inspection for Industrial Applications IX, SPIE, 2022, p. 98.
13. A. Ziad, E. Aristidi, J. Chabé, Y. Fanteï-Caujolle, C. Renaud, and C. Giordano, in Adaptive Optics Systems VII, SPIE, 2020, p. 1502.
14. E. Masciadri, J. Vernin, and P. Bougeault, Astro. Astrophys. Supplem. Ser. **137**, 185 (1999).
15. J. R. Beck, J. P. Bos, T. J. Brennan, and M. F. Spencer, Opt. Engin. **61**, 044104 (2022).
16. M. Xu, S. Shao, Q. Liu, G. Sun, Y. Han, and N. Weng, Appl. Sci. **11**, 8523 (2021).
17. X. Liu, Doctor of Philosophy Thesis, The University of Durham, (2021).
18. C. Schwab, Doctor of Natural Sciences Thesis, University of Heidelberg, (2010).
19. M. Carbillet, C. Verinaud, M. Guarracino, L. Fini, O. Lardiere, B. Le Roux, A. T. Puglisi, B. Femenia, A. Riccardi, and B. Anconelli, in Advancements in Adaptive Optics, SPIE, 2004, p. 637.
20. H. W. Shepherd, Doctor of Philosophy Thesis, Durham University, (2012).
21. R. N. Hassan, Doctor of Philosophy Thesis, University of Baghdad, (2012).

22. N. Ageorges and C. Dainty, *Laser guide star adaptive optics for astronomy*. Vol. 551. (Dordrecht; Boston, Springer Science & Business Media, 2013).
23. M. Bass, *Handbook of Optics: Volume V–Atmospheric Optics, Modulators, Fiber Optics, X-Ray and Neutron Optics*. Vol. V. 3rd Ed. (USA, McGraw-Hill Education, 2010).
24. M. K. Mardan, Doctor of Philosophy Thesis, University of Baghdad, (2018).
25. W. H. Wadee, Doctor of Philosophy Thesis, University of Baghdad, (2016).
26. R. Bracewell, *The Fourier Transform and Its Applications*. 3rd Ed. (Boston, McGraw-Hill, 2000).
27. N. Schnitzer, S. H. Sung, and R. Hovden, Micro. Microanal. **26**, 921 (2020).
28. M. K. Mirdan, R. N. Hassan, and B. Q. Al-Aboodi, Karbala Inter. J. Mod. Sci. **8**, 306 (2022).
29. A. Quirrenbach, Adap. Opt. Vis. Sci. Astro. **31**, 137 (2006).
30. Z. Wu, A. Iqbal, and F. B. Amara, *Modeling and Control of Magnetic Fluid Deformable Mirrors for Adaptive Optics Systems*. (Berlin, Germany, Springer, 2012).
31. H.-X. Yan, S.-S. Li, D.-L. Zhang, and S. Chen, Appl. Opt. **39**, 3023 (2000).
32. F. Ferreira, E. Gendron, G. Rousset, and D. Gratadour, Astro. Astrophys. **616**, A102 (2018).
33. F. Y. Kanev, V. V. Lukin, and N. A. Makenova, in 5th International Workshop on Adaptive Optics for Industry and Medicine, SPIE, 2006, p. 139.
34. A. Gurvich and M. Belen'kii, J. Opt. Soci. Amer. A **12**, 2517 (1995).
35. M. Chen, T. Gao, S. Hu, Q. Zeng, L. Liu, and G. Li, Resul. Phys. **7**, 3596 (2017).
36. R. D. Haameid, B. Q. Al-Abudi, and R. N. Hassan, Iraqi J. Sci. **62**, 5008 (2021).
37. A. Y. Shikhovtsev, P. G. Kovadlo, E. A. Kopylov, M. A. Ibrahimov, S. A. Ehgamberdiev, and Y. A. Tillayev, Atmosph. **12**, 1614 (2021).
38. M. C. Britton, in Advancements in Adaptive Optics, Glasgow, United Kingdom SPIE, 2004, p. 609.
39. K. Ahn, S.-H. Lee, I.-K. Park, and H.-S. Yang, J. Korean Phys. Soci. **79**, 918 (2021).
40. D. A. Paulson, Doctor of Philosophy Thesis, University of Maryland, College Park, (2020).
41. G. Agapito, A. Puglisi, and S. Esposito, in Adaptive Optics Systems V, Edinburgh, United Kingdom SPIE, 2016, p. 2164.
42. L. K. Abood, S. M. Al-Hilly, and R. N. Hassan, Iraqi J. Sci. **54**, 222 (2013).
43. R. N. Hassan and H. S. Ali, Karbala Intern. J. Mod. Sci. **9**, 3 (2023).
44. S. Gladysz, J. C. Christou, L. W. Bradford, and L. C. Roberts, Publ. Astron. Soci. Pacif. **120**, 1132 (2008).
45. D. Schmidt, T. Rimmele, J. Marino, and F. Wöger, Adapt. Opt. Syst. V **9909**, 316 (2016).
46. C. Li, Y. Lu, and S. Zhang, Opt. Engin. **60**, 073107 (2021).
47. M. Hart and J. L. Codona, in Unconventional Imaging and Wavefront Sensing 2012, SPIE, 2012, p. 122.
48. J. M. Beckers, Ann. Rev. Astro. Astrophys. **31**, 13 (1993).
49. F. Quirós-Pacheco, Doctor of Philosophy Thesis, Imperial College, (2006).
50. S. Ströbele, M. Kasper, and P.-Y. Madec, in Adaptive Optics Systems VII, Online Only SPIE, 2020, p. 270.

التحقيق في المحاكاة العددية لنظام البصريات التكيفية

سارة اسامة جاسم[1] و رائد نوفي حسان[1]
[1] قسم الفلك والفضاء، كلية العلوم، جامعة بغداد، بغداد، العراق

الخلاصة

في هذه الدراسة، تم تحليل أداء نظام البصريات التكيفية (AO) من خلال نمذجة رقمية باستخدام محاكاة حاسوبية ببرنامج MATLAB. تم إنشاء شاشة طور عن طريق تحويل أرقام عشوائية مولدة بالحاسوب إلى مجموعات ثنائية الأبعاد من قيم الطور على شبكة نقاط بنفس الإحصائيات الخاصة بتغيرات الطور الناجمة عن الاضطراب. تم إنشاء اضطراب فون كارمان اعتمادًا على كثافة الطيف الطاقوي. لتصوير شدة الاضطرابات الجوية، تم استخدام عدد من دوال الانتشار النقطية المحاكاة (PSFs) ودالة نقل التظمين (MTFs) لقيم مختلفة لقطر الانتشار المتجانس لفريد (r_o). لتقييم فعالية النظام البصري (التلسكوب)، تم حساب معدل ستريل (S). تم تنفيذ إجراء المكافأة والتعويض في نظام AO. باستخدام تحليل تحليلي لتحديد جبهة الموجية والزيوغ المتعلقة بفتحة التلسكوب الدائرية، تم استخدام متعددات زيرنايك لوصف الخطأ المتبقي وتحديد مدى تأثير المكافأة والتعويض على القيم المقاسة للاضطراب. أظهرت نتائج المحاكاة الحاسوبية للاضطرابات الجوية أن زيادة قيم r_o (4، 8، 12، 16، 20، 24، 28، 32) سم، أدت إلى زيادة S بنسبة 3.4٪. ولكن عندما تشغيل نظام البصريات التكيفية (AO) مع قيمة ثابتة ل r_o (20 سم) وبزيادة انماط الزيوغ لزيرنايك زادت S بنسبة 44٪ وهو تحسن كبير في عملية التعويض والمكافئة.

الكلمات المفتاحية: البصريات التكيفية، الكثافة الطيفية للطاقة، اضطراب Von Karman، متعدد الحدود Zernike، الاضطرابات الجوية.